# Cation Induced Changes to the Structure of Cryptophane Cages

## Supplementary Information

Oscar H. Lloyd Williams,[a] Claudia S. Cox,[a] Meng Yuan Zhang,[a] Martina Lessio,[a] Olivia Rusli,[a] William A. Donald,[a] Lachlan Jekimovs,[b] David L Marshall,[c] Michael C. Pfrunder,[b,d] Berwyck LJ. Poad,[b,c] Thierry Brotin,[e] and Nicole J. Rijs.[a]*

a) School of Chemistry, UNSW Sydney, Sydney, NSW, 2052, Australia

b) School of Chemistry and Physics, Queensland University of Technology, Brisbane 4001, Queensland, Australia

c) Central Analytical Research Facility, Queensland University of Technology, Brisbane, 4001 Australia

d) Centre for Materials Science, Queensland University of Technology, Brisbane, 4001 Australia

e) ENS Lyon, CNRS, Laboratoire de Chimie, UMR 5182, 46 Allée d'Italie, 69364 Lyon, France
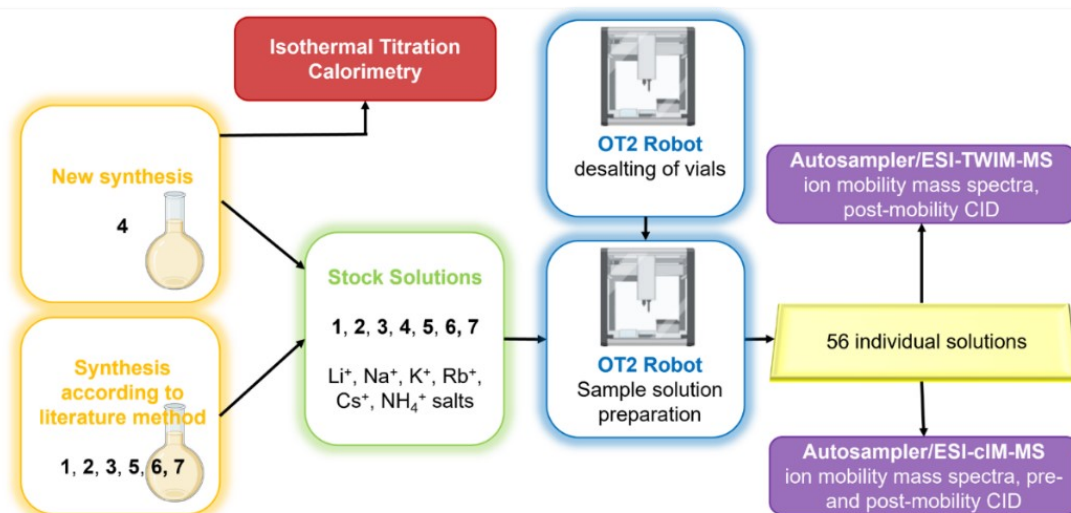
# Contents

# Methods



Figure S1: Experimental workflow for the library of cryptophane complexes.

## Synthesis of Cryptophanes 1-3, and 5-7

The cryptophanes were synthesized according to established literature methods. Namely, cryptophane-A was prepared by a stepwise synthesis from vanillyl alcohol.[8] Cryptophanes **1**, **2**, **3** and **5** were synthesized using cryptophane-A as the starting material.[1–3] Cryptophane **6** was prepared using a Sc(OTf)$_3$ reagent as described by Chapellet *et al*,[4,5] and Cryptophane **7** was prepared according to Brotin *et al*.[6]

## Synthesis of Cryptophane 4

Cryptophane **4** was prepared in 3 steps from cryptophane-224 (**8**) whose synthesis has been previously reported (Supporting Information, Scheme S1).[7] Demethylation of the six methoxy groups was performed using freshly prepared PPh$_2$Li (1M) in THF resulting in the expected cryptophane 4 in excellent yield (98 %).[8] Cryptophane **4** was allowed to react with acetic anhydride in pyridine to give rise to cryptophane 9 in 98% yield (Supporting Information, Scheme S1). The $^1$H NMR spectrum of compound 9 (Supporting Information, Figure S3) reveals the presence of two conformations; the expected globular form (main product) and the imploded form (secondary product). Hydrolysis of the ester functions in a KOH/H$_2$O(0.5 M)/THF mixture allows recovery of cryptophane 4 as a beige compound in 54 % yield. Cryptophane 4 is present only in globular form. Additional synthetic detail and characterization data is recorded in the Supporting Information (Synthetic Details and Characterization, Figures S4-S6).
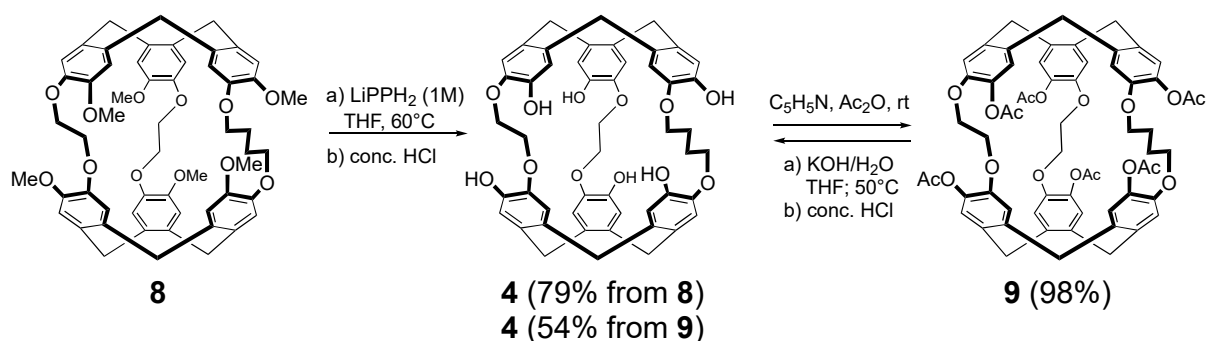


Scheme S1: The synthetic procedure of 4, starting from cryptophane-224 (**8**) and the additional synthetic step to **9**.

## Materials

Lithium Chloride (99.98% trace metal basis), potassium chloride (99.999% trace metal basis), sodium chloride (99.999% trace metal basis), rubidium chloride (99.95% trace metal basis), cesium chloride

(99.999% trace metal basis) and ammonium chloride (99.998%) were obtained from Sigma-Aldrich. These chemicals were used as supplied without further purification. Cryptophanes were used as synthesised (above).

## Sample Preparation

Glassware was soaked for 24h in 10% acetic acid, then robotically rinsed with water and methanol prior to use. Individual stock solutions of seven cryptophanes and six cations (**1-7**, $Li^+$, $Na^+$, $K^+$, $Rb^+$, $Cs^+$ and $NH_4^+$) were robotically prepared in 50:50 water: methanol in desalted vials. These stock solutions were then used to robotically prepare sample solutions with each cryptophane and each cation in a 1:1 molar ratio (7 cryptophanes x 7 cations = 49 sample solutions), plus 7 samples of cations with no cryptophanes, giving a total of 56 sample solutions. The concentration of final sample solutions is 50 μM (cryptophane).

## Ion Mobility-Mass Spectrometry

Experiments were performed either on (i) a SELECT SERIES Cyclic IMS (Waters,[9] Manchester, UK) to perform cyclic ion mobility mass spectrometry experiments or (ii) a Vion TWIMS Q-time of flight (ToF) (Waters, Manchester, UK), to perform standard TWIMS experiments, including collisional cross sections.

For the Vion TWIMS, the wave height in the travelling wave cell was nominally set to 15 V and the wave velocity to 300 m/s. The mass window (*m/z* 50 – 2000), gas controls, and all other instrument settings were set to the same values for all comparative experiments. A collisional cross section calibration was performed using a polyalanine solution (Polyalanine Calibration and Uncertainty Calculation S20).

For the Cyclic IMS, the wave height in the travelling wave cell was set to 20V and the wave velocity to 500 m/s. The number of passes the ions experienced was varied by increasing the time taken before the array was switched to transmission, from 5 ms to 50 ms to 130 ms. As the approximate time it takes for an ion to traverse the cyclic region (with the above settings) was *ca.* 40 ms, this resulted in 1 pass, 2 pass and 5 passes (although sometimes 6 passes were observed for smaller, faster complexes). The mass window (*m/z* 50 – 2000), gas controls, mass selected ion, and all other instrument settings were set the same for all comparative experiments.

## Electrospray Ionisation and Sample Introduction

For the Vion TWIMS, a standard electrospray ionization (ESI) source with a Waters Acuity I-Class UPLC (as an autoinjector) with a methanol flow rate of 0.2 μL/min and a source temperature of 120 °C and a spray voltage of 2kV were used. Each experiment was performed in duplicate.

For the Cyclic IMS, a standard electrospray ionization (ESI) source with a Waters Acuity I-Class UPLC (as an autoinjector) with a methanol flow rate of 0.2 μL/min and a typical source temperature of 100°C and a spray voltage of 2 kV was used. The source conditions were tuned to allow the formation of the complexes and were held constant unless otherwise stated. Samples were introduced via loop injection from a UPLC.

In the absence of salt, electrospray ionization of cryptophanes **1 – 7** (Scheme 2 and 3) yielded protonated [cryptophane+H]+ species in the positive ion mass spectrum. Positive ESI MS of 1:1 solutions of cryptophanes **1-7** and $Li^+$, $Na^+$, $K^+$, $Rb^+$, $Cs^+$ and ammonium salts (Figure 1) resulted in the formation of a dominant ion at the mass to charge ratio (*m/z*) of the [cation+cryptophane]+ species for each (Eq. 1). Nonspecific dimers, complexes of other stoichiometries, salt clusters or solvent adducts were not observed in any of the mass spectra.

## Low Energy Collision Induced Dissociation

To gain further insight into both the stability and connectivity of the host-guest species, several species were analysed via low energy collision induced dissociation (CID). Simple cryptophanes **1** and **2** were used to "tune" a suitable collision energy in both the trap and transfer region of the cyclic ion mobility instrument (Figure S8).[9] The minimum onset collision voltage required to produce a fragment ions was nominally 80 volts for all species (rather than adjusting for individual species). For the cyclic, MS/MS experiments were automatically generated via a python script (https://zenodo.org/doi/10.5281/zenodo.11174559).

## Isothermal Titration Calorimetry

Isothermal Titration Calorimetry (ITC) experiments were performed at 298 K. In a standard experiment, the host solution (~ 0.1 mM) in LiOH (0.1 M), NaOH (0.1 M) was placed into the calorimeter cell (1.4 mL) and 28 successive aliquots (10 μL) of guest solution (10 times more concentrated) were added via a computer-automated injector at 3 min intervals. Heat changes were recorded after each addition. Heats of dilution were measured by a blank experiment (in absence of host) under the same conditions, and they were subtracted from the titration data prior to curve fitting. The first injection was discarded from each data set to remove the effect of guest diffusion across the syringe tip during the equilibration process. Titration curves were fitted

using the single binding site model or a competitive binding model (competition experiments). The use of a competitor (RbCl) was mandatory in cases where binding constants were too high to be measured accurately.

## Electronic Structure Calculations

To predict the structure of the cryptophane host-guest complexes, Kohn-Sham density functional theory (DF) as implemented in Orca v5.0 software was utilized.[10] The gas phase structures of protonated cryptophane complexes as well as complexes of cryptophanes with alkali metal (Li, Na, K, Rb and Cs) and ammonium ($NH_4^+$) cations were optimized using the ωB97X-D3BJ functional with def2-SVP geometry optimization (def2-TZVPP on all non-hydrogen guest atoms) and def2-TZVPP single point refinement (ma-def2-TZVPP on all non-hydrogen guest atoms).

Imploded structures were optimized for cryptophane **1** and cations = H, Li, Na, K, Rb, and Cs. The cation was placed in 3 locations – as per Figure 5.

For cryptophanes **1-4**, an optimized structure was generated for the cation in both interior and exterior positions. Two exterior positions were chosen, and one interior position was chosen as described in the Discussion section of the main text. The calculated collision cross sections of each optimized structure are recorded in Table 1 and 3, with the Tl data reported in Table S8. Additionally, reaction energies were calculated using (eq. 6).[11]

$$\Delta E \quad = \quad E_{complex} - E_{cryptophane} - E_{cation} \quad (6)$$

This describes the change in energy of the separated reactants ($E_{cation}$, and $E_{cryptophane}$) forming the complex, $E_{complex}$ (whether encapsulated or not). These energy values are negative (exothermic) as the complexes are more stable than their separated cryptophanes and cations. An increasingly negative value denotes an increasingly strong interaction which can be linked to electronic stability. When the cation in the species was a proton, a modified equation (eq. 7) is used.

$$\Delta E \quad = \quad E_{complex} - E_{cryptophane} \quad (7)$$

These energy calculations were performed without implicit or explicit solvation and are based on $E_0$ values. Therefore, whilst the gas phase energetics are appropriate for comparison of the gas phase structures, caution must be applied to interpretation of solution phase energetics, where solvent effects and Gibbs free energy must be considered.

Theoretical comparison with Thallium was undertaken, due to interest in applicability toward the cation (Page S21).

## Collisional cross section calculations

From the DFT generated geometries, $N_2$ collision cross-sections were calculated using the trajectory method in the IMoS program (v1.10).[12–15] As others have also observed,[16] a systematic 10% offset between the experimental and theoretically predicted Ω values was noted. A scaling factor of 0.9 was applied to account for a consistent systematic offset between experimental and theoretical cross sections.

Throughout this work this scaled value is referred to as $\Omega_{calc}$ (the unscaled values are recorded in Supporting Information S23). Applying a scaling factor should not be done without due consideration of the root causes for the offset .

## Cavity Volume Calculations

Existing approaches to determine molecular cavity volumes, center on assessing the cavities within crystallographic structures.[17] A fit-for-purpose method was devised here that estimates cavity volume from gas phase DFT optimized structure. In general, a simple, small cavity (i.e., one with a relatively simple topology e.g., spherical and single guest encapsulation) should be best described as a convex volume of space (Figure S1a). A convex volume is one in which any point can be accessed from any other point within the volume without passing through the bounding surface, or more simply put, "bulging with no dents". A concave shape, (where the surface is not convex) suggests a protrusion or "dent" into the cavity, which, when the cavity is small, will be the actual bound of the cavity (Figure S1a, atom vii). A larger cavity, such as those found in biomolecules, may be better described by a concave cavity, which is beyond the scope of this approach (Figure S1b).

In the optimized structures, the cavity was visibly bounded by the planar aromatic groups of the cyclotribenzylene groups, which sat as planes on the surface of the cavity. These 36 carbon atoms defined the volume of the cavity (Figure S2). Using the ConvexHull Scipy Package in Python, the convex hull (the smallest volume defined by these points) was calculated. However, this hull is defined by the nuclear

coordinates and so is an overestimate of the cavity volume. Accounting for this, the points were translated 1.7 Å towards the center of the cavity. This represents a carbon atom's Van der Waals radius. The new cavity is significantly smaller but represents the volume of space a guest could exist in (Figure S2). This method does not account for any flexibility, bonding, or temperature effects. The bounding atoms were selected by visual inspection. To generalize this approach, one should endeavor find the largest convex hull which contains no atomic centers after accounting for Van der Waals radii. Additional details are given in Volume Calculation Validity S29.
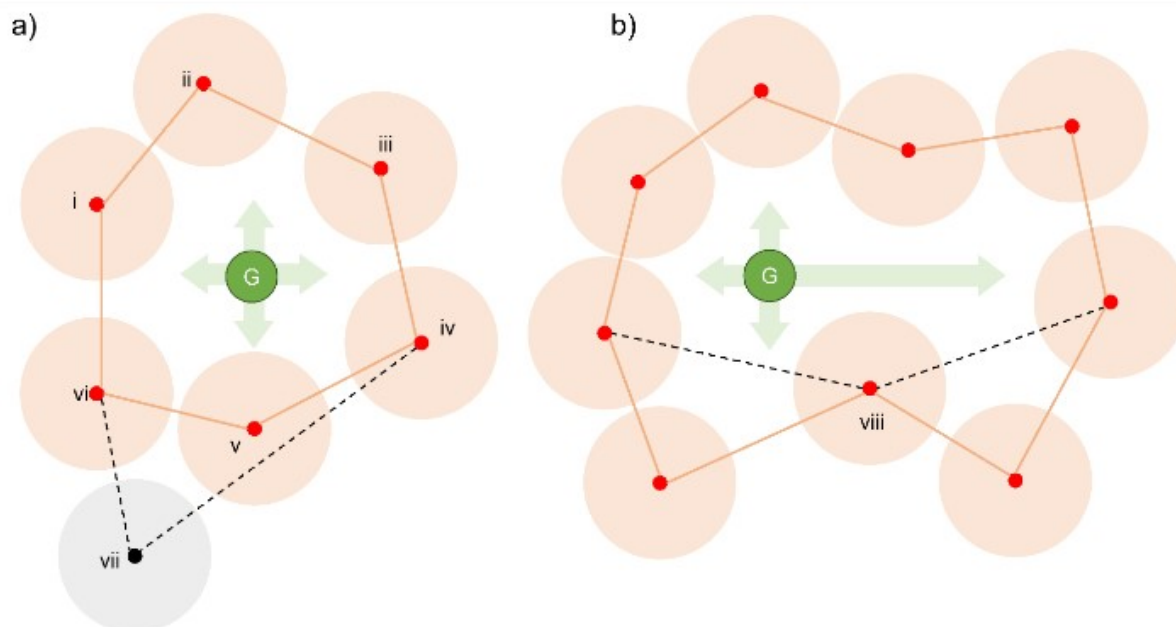


Figure S2: The two shape-based approach to determining cavity volume, illustrated with 2-dimensional approximations where red points represent nuclei and the larger diameter circles represent van der Waals radii, with a guest molecule "G" (green) incorporated within the cavity. a) The convex approach. This finds the largest convex volume defined without any points being within the volume. In this case, atoms i-vi define this region. If vii is added to the bounding atoms, then atom v would be incorporated within the volume or would create a bounding surface that would break convexity. It is also worth noting that visually, the VDW radius of vii does not cross the bounding surface of the convex volume, suggesting it does not impact the cavity. b) A concave cavity, by comparison represents a larger, irregular cavity where a convex shape defined using atom viii may exclude cavity volume (dashed black lines) and so a concave cavity is a more appropriate definition.
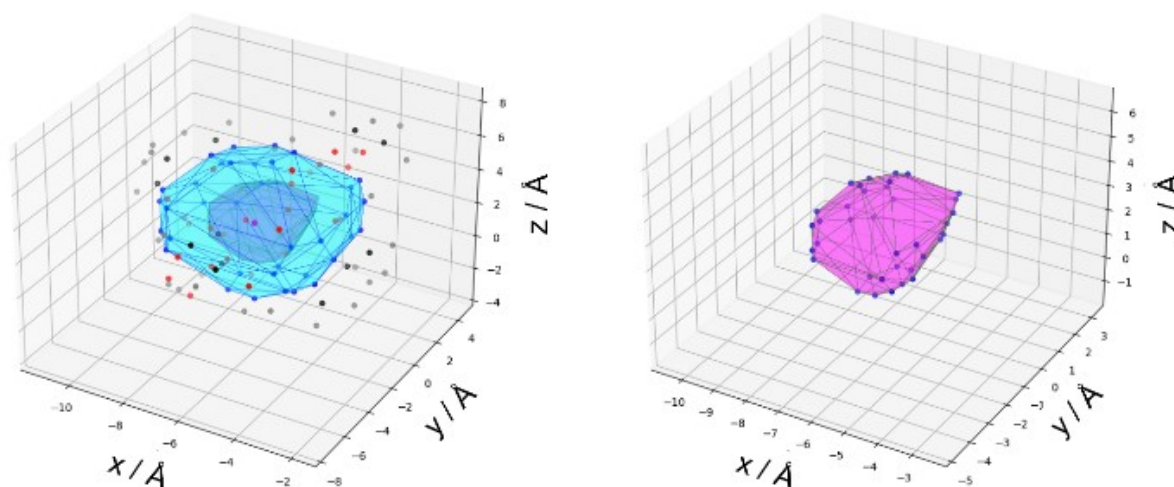


Figure S3: Molecular volumes' generated by Python Script. The hull defined by a) the aromatic carbons is significantly larger than the hull defined by b) the Van der Waals radii adjusted points. Note in a) all atoms are shown with the aromatic carbons defining the cavity shown in blue.

## Additional Synthetic Details and Characterization

### Synthesis of Cryptophane 4

Lithium diphenylphosphide (1M; 6.5 mL) was added via a syringe to a solution of cryptophane-224 (**8**; 0.3 g, 0.33 mmol) in dry THF (3 mL) under an argon atmosphere. The dark red solution was stirred for 48 hours at 60°C.  Then, the solution was poured into water (20 mL). The aqueous solution was then washed five times with $CH_2Cl_2$ and then acidified with conc. HCl resulting in a precipitate. The solid was collected on a frit and washed with water, dried on air and then washed several times with diethyl ether to give **4** as a white solid (0.22 g, 79%). The compound is clean by NMR but to ensure the purity of **4** an additional purification step was applied. Thus, compound **4** (0.22 g, 0.26 mmol) was dissolved in dry pyridine (5 mL) under an argon atmosphere. The stirred solution was cooled to 0° C with an ice bath, then an excess of acetic anhydride (1.4 mL) was introduced via a syringe. The solution was stirred for 16 hours at room temperature (20-25° C). Then, the solution was poured into a mixture of water (20 mL) and $CH_2Cl_2$ (20 mL). The aqueous phase was stirred three times with $CH_2Cl_2$. The combined organic layers were washed once with water and then dried over $Na_2SO_4$. Evaporation of the solvent under reduced pressure gives rise to a white solid. Purification on silica gel ($CH_2Cl_2$/Acetone: 90/10) gives compound **9** as a white solid (0.28 g, 98 %). $^1H$ NMR (300 MHz, $CD_2Cl_2$, 25 °C): $\delta$ = 6.97 (s, 2H), 6.92 (s, 2H), 6.90 (s, 2H), 6.85 (s, 2H), 6.82 (s, 4H), 4.65 (d, $J$ = 13.5 Hz, 2H), 4.63 (d, $J$ = 13.5 Hz, 2H), 4.60 (d, $J$ = 13.5 Hz, 2H), 4.32-4.04 (10H, m), 3.62 (2H, m), 3.53 (d, $J$ = 13.5 Hz, 2H), 3.50 (d, $J$ = 13.5 Hz, 4H), 2.42 (s, 6H), 2.31 (s, 6H), 2.27 (s, 6H), 2.00-1.70 (4H, m). $^{13}C\{^1H\}$ NMR (75.5 MHz, $CD_2Cl_2$, 25 °C): $\delta$ 169.3 (2$C$), 169.0 (2$C$), 168.95 (2$C$), 149.8 (2$C$), 149.0 (2$C$), 148.9 (2$C$), 140.9 (2$C$), 140.5 (2$C$), 140.0 (2$C$), 138.6 (2$C$), 138.1 (2$C$), 137.8 (2$C$), 134.4 (2$C$), 133.3 (2$C$), 132.6 (2$C$), 124.9 (2$C$), 124.8 (2$C$), 124.1 (2$C$), 121.4 (2$C$), 118.8 (2$C$), 118.3 (2$C$), 69.5 (2$C$), 69.0 (2$C$), 68.7 (2$C$), 36.6 (6$C$), 25.0 (2$C$), 21.2 (4$C$), 21.0 (2$C$). HRMS (ESI) m/z: $[M+Na]^+$ Calcd for $C_{62}H_{58}NaO_{18}$ 1113.3515; Found. 1113.3505

Compound **9** (0.28 g, 0.26 mmol) was added to a solution of THF (7 mL) and $KOH/H_2O$ solution (0.5 M; 7 mL). The heterogeneous mixture was stirred overnight at 50° C under an argon atmosphere. Then, the THF solution was evaporated under reduced pressure and water (10 mL) was added. The solution was then acidified with few drops of conc. HCL to give rise to a white solid, which was washed with water and then dried in air. Then, the solid was washed several times with diethyl ether to give compound **4** as a white precipitate (0.13 g, 54 %). $^1H$ NMR (300 MHz, DMSO-$d_6$, 25 °C): $\delta$ = 8.78 (s, 2H), 8.37 (s, 2H), 8.31 (s, 2H), 6.92 (s, 2H), 6.74 (s, 2H), 6.71 (s, 2H), 6.65 (s, 2H), 6.62 (s, 2H), 6.54 (s, 2H), 4.49 (d, $J$ = 13.5 Hz, 2H), 4.42 (2H, m), 4.41 (d, $J$ = 13.5 Hz, 4H), 4.20-3.90 (8H, m), 3.71 (2H, m), 3.20 (d, $J$ = 13.5 Hz, 4H), 3.185 (d, $J$ = 13.5 Hz, 2H), 1.50 (4H, m). $^{13}C\{^1H\}$ NMR (75.5 MHz, DMSO-$d_6$, 25 °C): $\delta$ 146.6 (2$C$), 146.0 (2$C$), 144.9 (2$C$), 144.8 (2$C$), 144.3 (2$C$), 143.4 (2$C$), 134.1 (2$C$), 133.3 (2$C$), 133.2 (2$C$), 131.4 (2$C$), 130.2 (2$C$), 129.1 (2$C$), 120.2 (2$C$), 118.8 (2$C$), 118.3 (2$C$), 117.5 (2$C$), 117.4 (2$C$), 116.8 (2$C$), 69.8 (2$C$), 68.3 (2$C$), 67.5 (2$C$), 35.0 (3$C$), 34.8 (3$C$), 25.1 (2$C$). HRMS (ESI) m/z: $[M+Cl]^-$ Calcd for $C_{50}H_{46}ClO_{12}$ 873.2683; Found.873.2690.
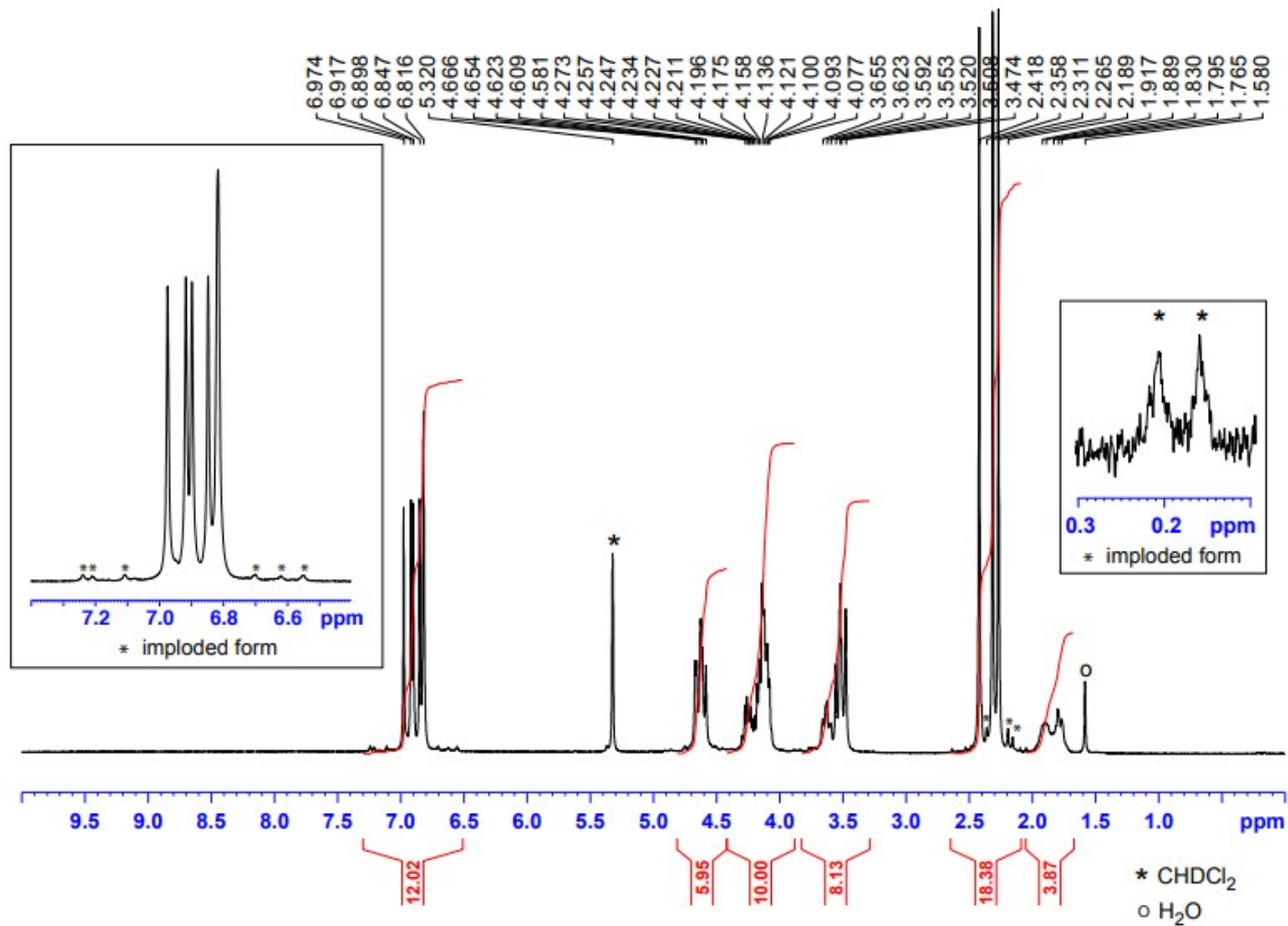
**NMR Spectra**



Figure S4: ¹H NMR (300 MHz) spectrum of *anti*-cryptophane-**9** recorded in CH₂Cl₂ at 298 K. The stars show NMR signals of the imploded form.
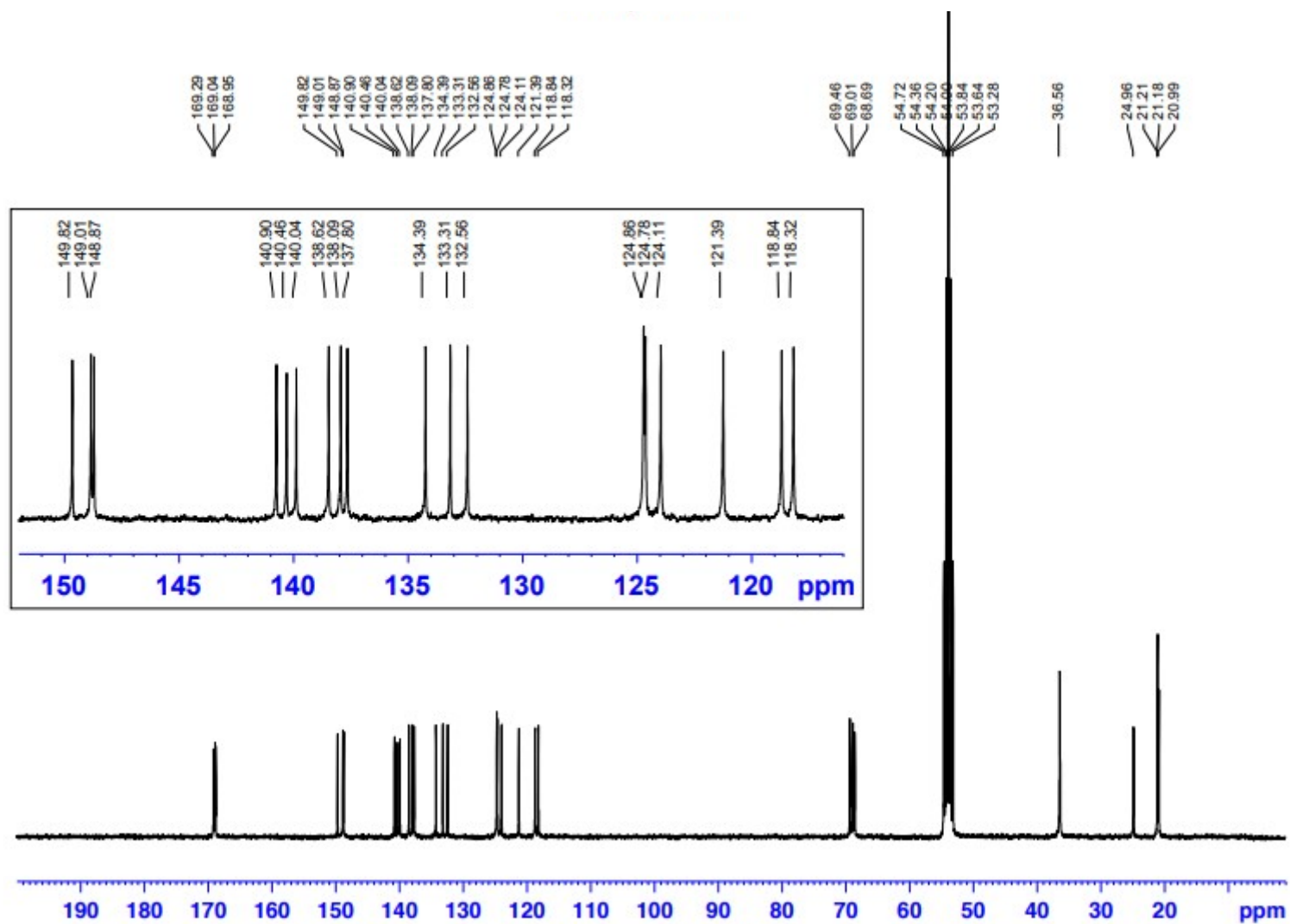
Figure S5: $^{13}$C NMR (75.5 MHz) spectrum of *anti*-cryptophane-**9** recorded in CH$_2$Cl$_2$ at 298 K.

S9

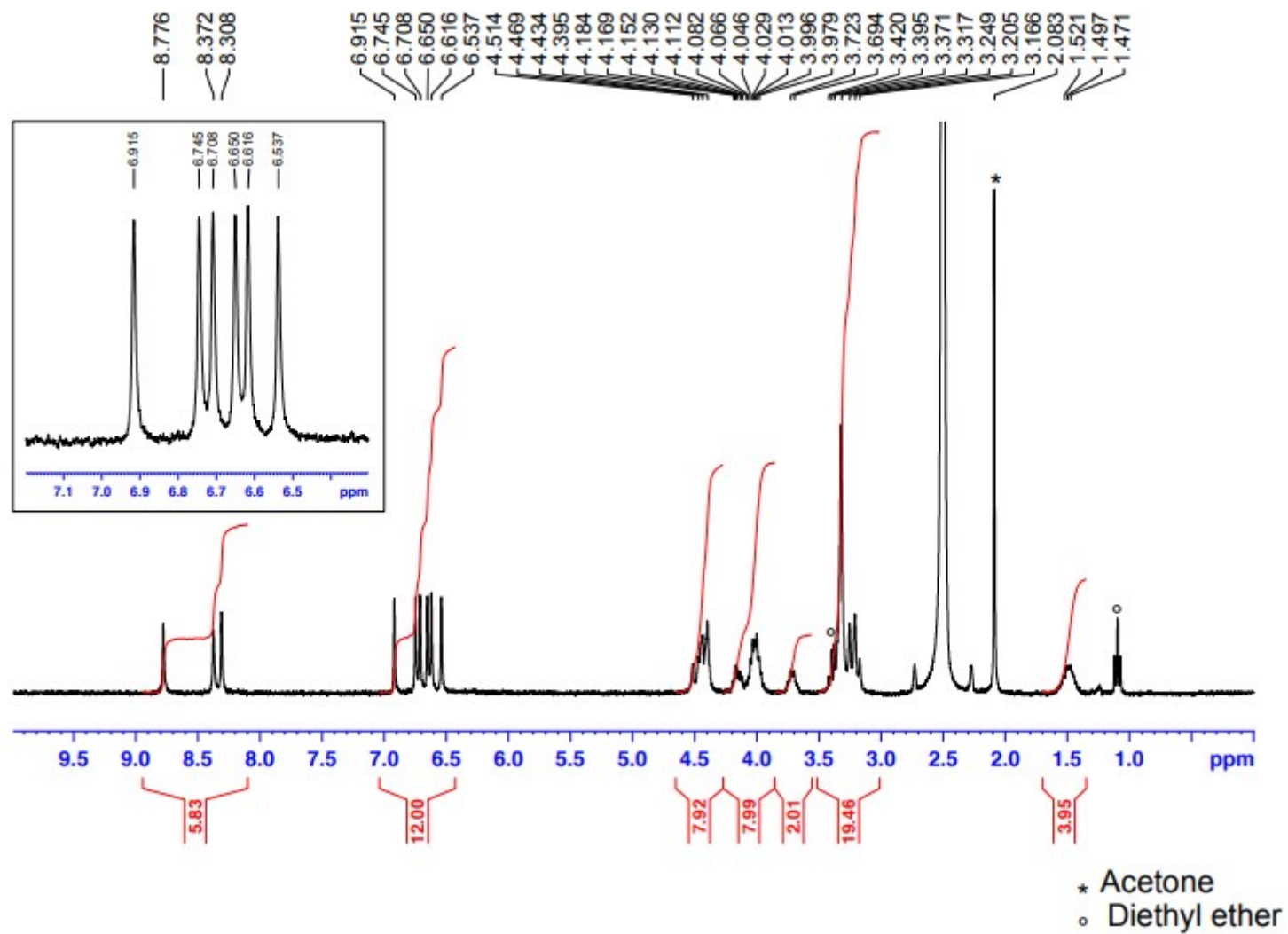Figure S6: ¹H NMR (300 MHz) spectrum of *anti*-cryptophane-**4** recorded in DMSO-$d_6$ at 298 K.
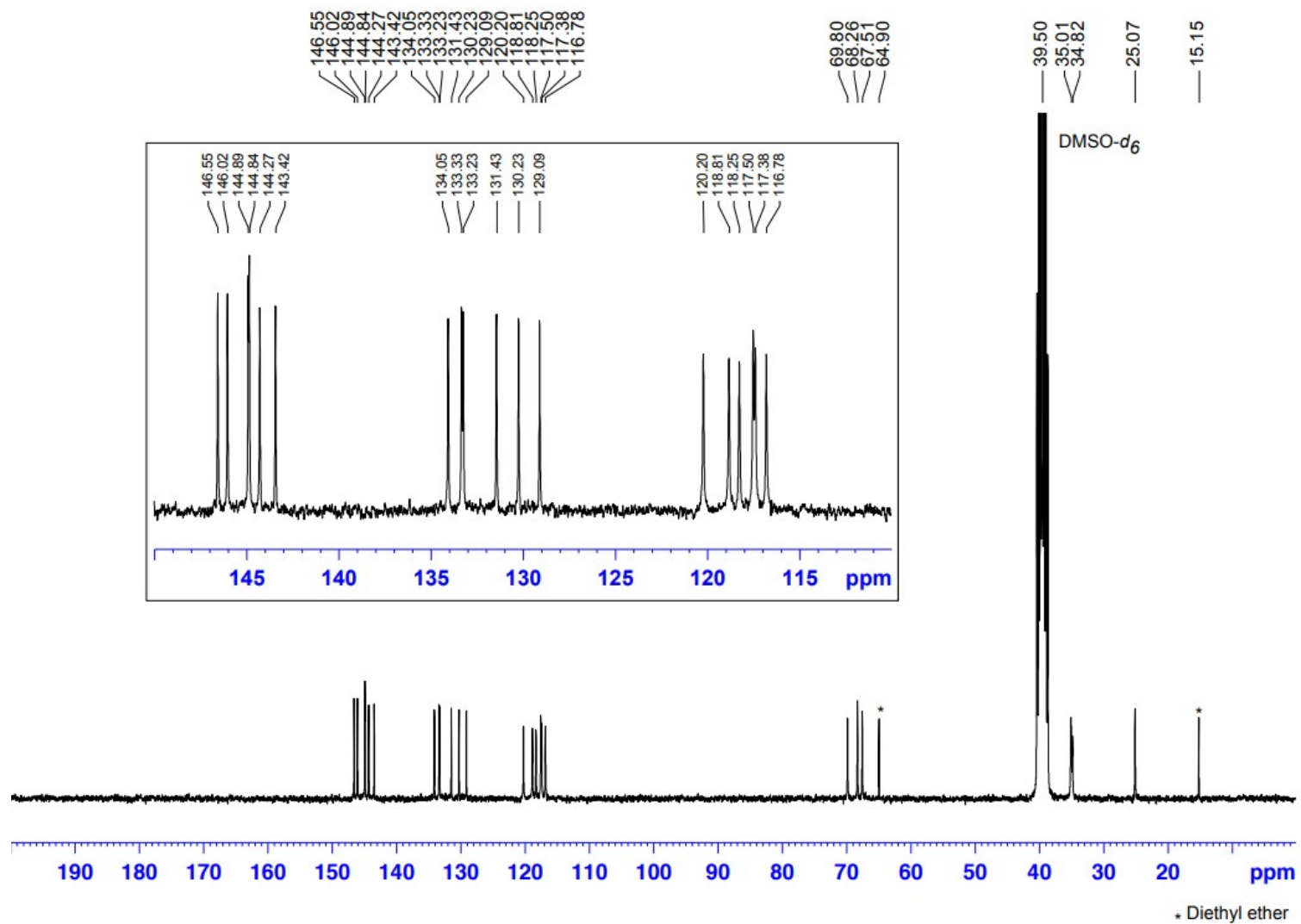
Figure S7: $^{13}$C NMR (75.5 MHz) spectrum of *anti*-cryptophane-**4** recorded in DMSO-$d_6$ at 298 K.

## Isothermal Calorimetry Data

### Tabulated Data

Tables S1 and S2 show the association constants measured in LiOH/$H_2O$ (0.1 M) and NaOH/$H_2O$ (0.1 M) for compound **4**, as well as the thermodynamic parameters of the complexation $\Delta H^0$, $\Delta S^0$ and $\Delta G^0$. Table S1 and Table S2 show that compound **4** binds well the alkali cation $Rb^+$ with a binding constant K = $1.9 \times 10^5$ $M^{-1}$ and K = $3.7 \times 10^5$ $M^{-1}$ in LiOH/$H_2O$ (0.1 M) and NaOH/$H_2O$ (0.1 M), respectively. Interestingly, compound **4** shows higher association constants with $Cs^+$ and $Tl^+$ by several orders of magnitude. For instance, association constants K = $7.5 \times 10^7$ $M^{-1}$ and $1.5 \times 10^{10}$ $M^{-1}$ were measured for $Cs^+$ and $Tl^+$ in LiOH/$H_2O$ (0.1 M), respectively. Notably, the same trend in their binding affinity $Tl^+ > Cs^+ \gg Rb^+$ was observed with compound **4** and the other cryptophanes **1-3** and **5-7**. For comparison, we have also reported in Table S1 and S2 the binding constants and the thermodynamic parameters of complexation of compound **1**, that represents to date the best cryptophane host for the encapsulation of $Tl^+$ and $Cs^+$.

**Table S1: Equilibrium constants, enthalpy entropy and Gibbs free energy values determined for 1, (from previous literature)[2] and 4 via isothermal calorimetry in LiOH (0.1 M) at 298 K.**

| Complexes | K / $M^{-1}$ | $\Delta H^0$ / kJ mol$^{-1}$ | $T\Delta S^0$ / kJ mol$^{-1}$ | $\Delta G^0$ / kJ mol$^{-1}$ |
|---|---|---|---|---|
| $Rb^+$@**1** | $9.2 \times 10^5$ | -25.1 | 8.8 | -33.9 |
| $Cs^+$@**1** | $2.7 \times 10^9$ | -55.6 | -1.7 | -53.9 |
| $Tl^+$@**1** | $5.0 \times 10^{10}$ | -53.5 | 7.5 | -61.0 |
| $Rb^+$@**4** | $1.9 \times 10^5$ | -22.5 | 7.5 | -30.0 |
| $Cs^+$@**4** | $7.5 \times 10^7$ | -44.0 | 1.0 | -45.0 |
| $Tl^+$@**4** | $1.5 \times 10^{10}$ | -51.0 | 7.0 | -58.0 |

**Table S2: Equilibrium constants, enthalpy entropy and Gibbs free energy values determined for 1 (from previous literature)[2] and 4 via isothermal calorimetry in NaOH (0.1 M) at 298 K.**

| Complexes | K ($M^{-1}$) | $\Delta H^0$ / kJ mol$^{-1}$ | $T\Delta S^0$ / kJ mol$^{-1}$ | $\Delta G^0$ / kJ mol$^{-1}$ |
|---|---|---|---|---|
| $Rb^+$@**1** | $1.4 \times 10^6$ | -23.8 | 11.2 | -35.1 |
| $Cs^+$@**1** | $4.4 \times 10^9$ | -56.9 | -1.6 | -55.3 |
| $Tl^+$@**1** | $6.2 \times 10^{10}$ | -51.4 | 10.1 | -61.5 |
| $Rb^+$@**4** | $3.7 \times 10^5$ | -18.6 | 13.2 | -31.8 |
| $Cs^+$@**4** | $6.9 \times 10^8$ | -41.4 | 9.1 | -50.5 |
| $Tl^+$@**4** | $3.2 \times 10^{10}$ | -47.7 | 12.1 | -59.8 |

**ITC Plots**



Figure S8**:** Calorimetric titration of **4** in LiOH/H$_2$O (0.1 M). The host solution (c= 98.6 mM) was placed into the calorimeter cell (1.4 mL) and 28 successive aliquots (10 mL) of RbCl solution (c=1023 mM) were added at 3 min intervals.



Figure S9: Calorimetric titration of **4** in LiOH/H$_2$O (0.1M). The host solution (c= 99.6 mM; was placed into the calorimeter cell (1.4 mL) and 28 successive aliquots (10 mL) of CsOH/H$_2$O solution (c=1020 mM) were added at 3 min intervals.

Figure S10: Competition experiment. Calorimetric titration of **4** in LiOH/$H_2O$ (0.1M). The host solution (c= 30 mM; was placed into the calorimeter cell (1.4 mL) and 28 successive aliquots (10 mL) of TlOAc solution (c= 393 mM) were added at 3 min intervals. The concentration of RbCl was c= 512 mM.
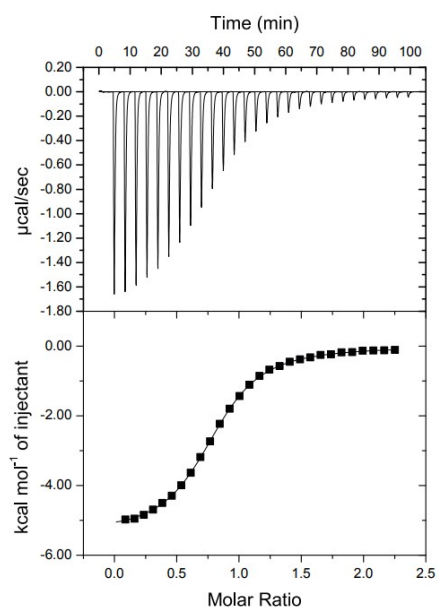


Figure S11: Calorimetric titration of **4** in NaOH/$H_2O$ (0.1 M). The host solution (c= 100 mM) was placed into the calorimeter cell (1.4 mL) and 28 successive aliquots (10 mL) of RbCl solution (c=1030 mM) were added at 3 min intervals.
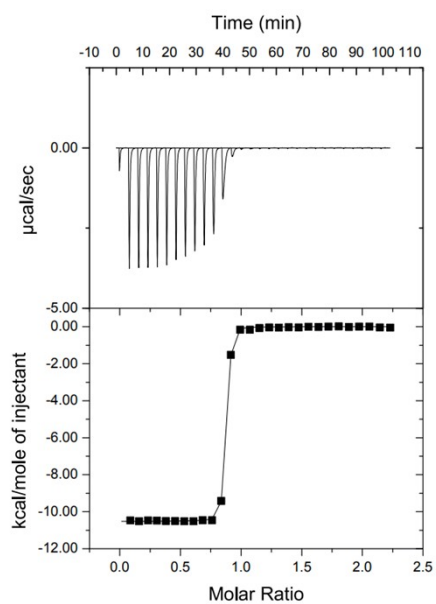
Figure S12: Calorimetric titration of **4** in NaOH/$H_2O$ (0.1M). The host solution (c= 29.8 mM; was placed into the calorimeter cell (1.4 mL) and 28 successive aliquots (10 mL) of CsOH/$H_2O$ solution (c=410 mM) were added at 3 min intervals. The concentration of RbCl was c= 300 mM.
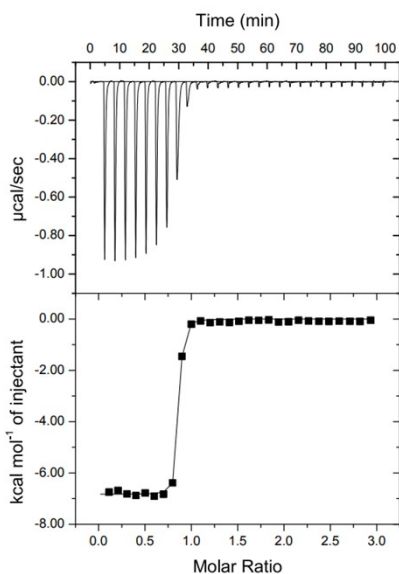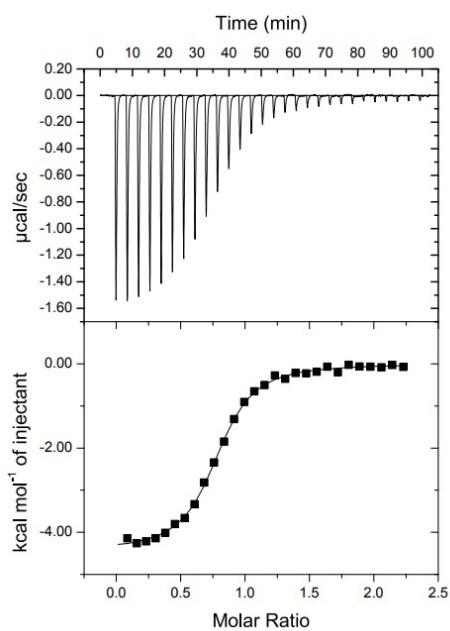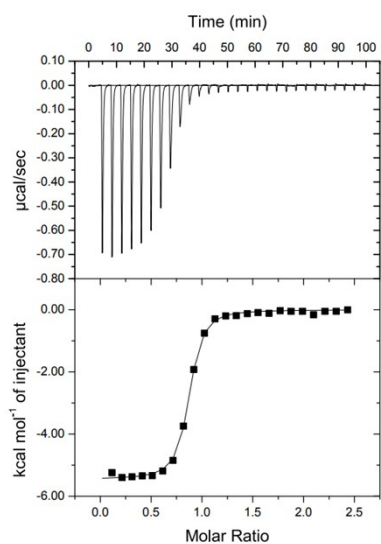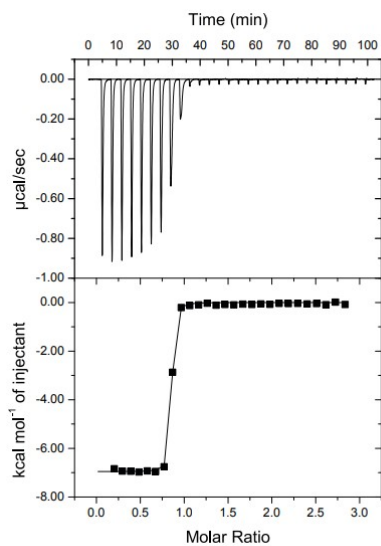


Figure S13: Calorimetric titration of **4** in NaOH/$H_2O$ (0.1M). The host solution (c= 30.1 mM; was placed into the calorimeter cell (1.4 mL) and 28 successive aliquots (10 mL) of TlOAc solution (c= 393 mM) were added at 3 min intervals. The concentration of RbCl was c= 893 mM.

## Measurements on Cyclic Ion Mobility Instrument
### Tabulated Data

**Table S3: Drift times and *m/z* values recorded on the cyclic IMS instrument for the main species in the sample. Analysis time started after 1 pass around cyclic ion mobility section.**

| Cation | 1 Drift time/ ms | m/z | 2 Drift time/ ms | m/z | 3 Drift time/ ms | m/z | 4 Drift time/ ms | m/z |
|---|---|---|---|---|---|---|---|---|
| $H^+$ | 41.73 | 811.27 | 40.71* | 825.29 | Not Observed | | 41.39 | 839.3 |
| $Li^+$ | 40.03 | 817.28 | 41.05 | 831.29 | 42.41 | 845.31 | 42.07 | 845.31 |
| $Na^+$ | 39.01 | 833.25 | 40.03 | 847.27 | 42.07 | 861.29 | 41.39 | 861.29 |
| $K^+$ | 38.67 | 849.23 | 40.03 | 863.24 | 41.73 | 877.26 | 41.39 | 877.26 |
| $Rb^+$ | 39.01 | 895.18 | 40.37 | 909.79 | 42.07 | 923.21 | 41.39 | 923.21 |
| $Cs^+$ | 39.35 | 943.17 | 40.71 | 957.18 | 42.41 | 971.20 | 41.73 | 971.20 |
| $NH_4^+$ | 38.67 | 828.30 | 40.03 | 842.32 | 41.73 | 856.33 | 41.05 | 856.33 |

*Low signal intensity

**Table S4: Drift time and *m/z* values recorded on the cyclic IMS instrument for the main species in the sample. Analysis time started after 2 passes around cyclic ion mobility section.**

| Cation | 1 Drift time/ ms | m/z | 2 Drift time/ ms | m/z | 3 Drift time/ ms | m/z | 4 Drift time/ ms | m/z |
|---|---|---|---|---|---|---|---|---|
| $H^+$ | 69.36 | 811.27 | 65.96* | 825.29 | Not Observed | | 68.51* | 839.30 |
| $Li^+$ | 65.11 | 817.28 | 67.66 | 831.3 | 70.21 | 845.32 | 69.36 | 845.32 |
| $Na^+$ | 63.41 | 833.26 | 65.96 | 847.27 | 69.36 | 861.29 | 67.66 | 861.29 |
| $K^+$ | 63.41 | 849.23 | 65.96 | 863.25 | 69.36 | 877.26 | 67.66 | 877.26 |
| $Rb^+$ | 63.41 | 895.18 | 65.96 | 909.19 | 69.36 | 923.21 | 68.51 | 923.21 |
| $Cs^+$ | 64.26 | 943.17 | 66.81 | 957.2 | 70.21 | 971.2 | 68.51 | 971.20 |
| $NH_4^+$ | 63.41 | 828.3 | 65.96 | 842.32 | 68.51 | 856.33 | 67.66 | 856.33 |

**Table S5: Drift time and *m/z* values recorded on the cyclic IMS instrument for the main species in the sample. Analysis time started after 5 passes around cyclic ion mobility section. The results obtained for $Na^+$, $K^+$ and $NH_4^+$ with 1 (marked with ▲) represent the species after 6 passes.**

| Cation | 1 Drift time/ ms | m/z | 2 Drift time/ ms | m/z | 3 Drift time/ ms | m/z | 4 Drift time/ ms | m/z |
|---|---|---|---|---|---|---|---|---|
| $H^+$ | 151.21 | 811.28 | 146.11* | 825.29 | Not Observed | | 150.36 | 839.31 |
| $Li^+$ | 143.56 | 817.28 | 148.66 | 831.30 | 154.61 | 845.32 | 152.91 | 845.32 |
| $Na^+$ | 164.81▲ | 833.26 | 146.11 | 847.27 | 153.76 | 861.29 | 150.36 | 861.29 |
| $K^+$ | 164.81▲ | 849.23 | 145.26 | 863.25 | 152.91 | 863.25 | 150.36 | 877.26 |
| $Rb^+$ | 142.71 | 895.18 | 146.96 | 909.19 | 153.76 | 923.21 | 151.21 | 923.21 |
| $Cs^+$ | 142.71 | 943.17 | 148.66 | 957.18 | 154.61 | 971.20 | 152.91 | 971.20 |
| $NH_4^+$ | 164.81▲ | 828.30 | 145.26 | 842.32 | 152.91 | 856.33 | 150.36 | 856.33 |

**Additional Cyclic IM Figures**
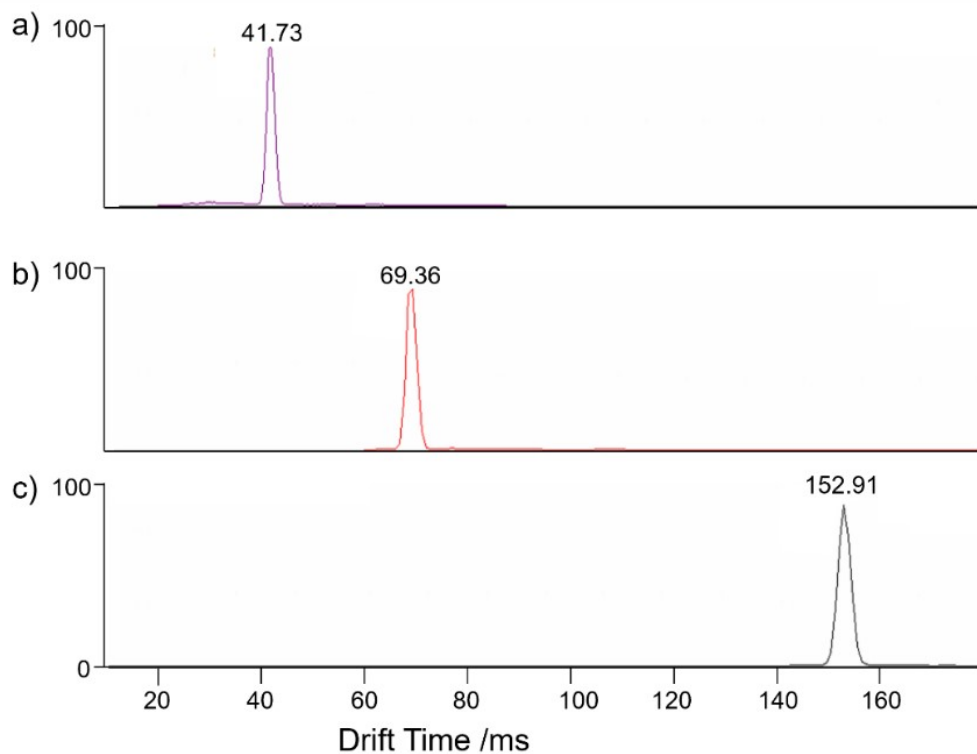


Figure S14: An increased number of passes does not significantly alter the peak shape of the [K+**3**]⁺ species. There is a noted broadening effect, which is derived from the electrostatic repulsion between ions within the ion packet.
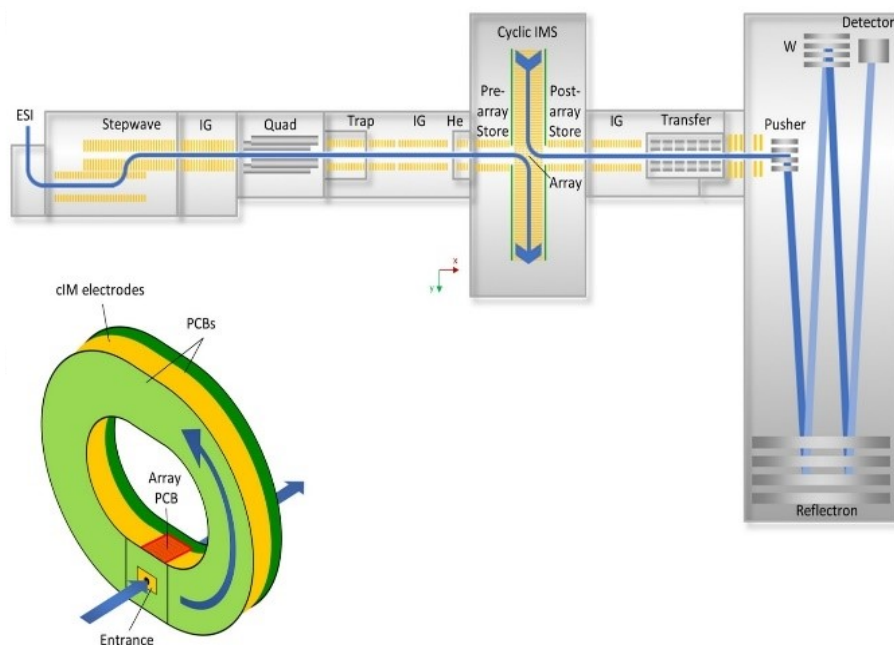


Figure S15: The layout of the cyclic ion mobility instrument. Note the location of the trap region. Reproduced from "A Cyclic Ion Mobility-Mass Spectrometry".[9]

Figure S16: Arrival time distributions of [Na+cryptophane]+ for 1-4.

## Polyalanine Calibration and Uncertainty Calculation

This calibration was done to support the automatic calibration carried out by the Vion and to allow an understanding of the error.

**Table S6: Literature values used for $\Omega_{exp}$ calibration compared to the drift time they were observed at.[18]**

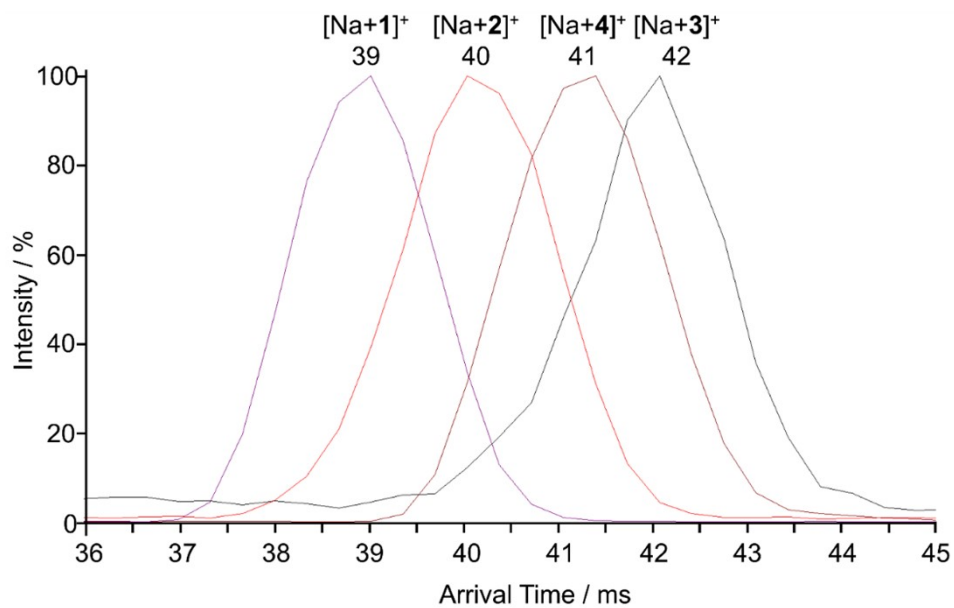| Polyalanine $\Omega_{lit}$ / Å$^2$ | Experimental drift time /ms |
|---|---|
| 166 | 3.63 |
| 195 | 4.74 |
| 211 | 5.33 |
| 228 | 5.97 |
| 243 | 6.49 |
| 256 | 6.94 |
| 271 | 7.42 |
| 282 | 7.88 |
| 294 | 8.32 |
| 306 | 8.71 |

**Table S7: Calculated statistics, including the uncertainty for the smallest value of $\Omega_{exp}$ measured, which provides the largest error.**

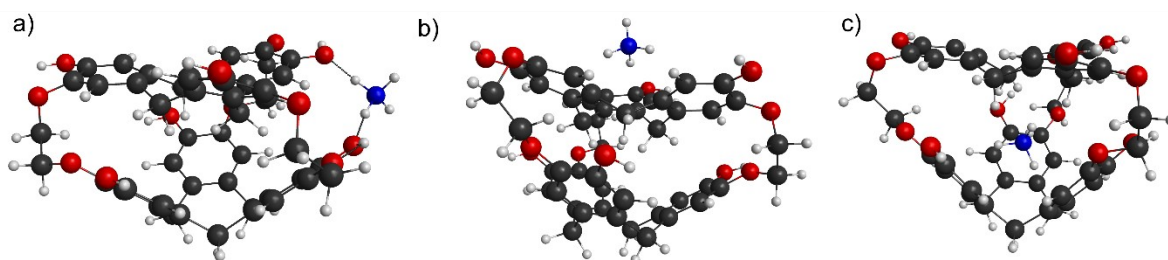| Statistic | Value (3 d.p) |
|---|---|
| Intercept (a) | -2.312 |
| slope (b) | 0.036 |
| s(a) | 0.066 |
| s(b) | 0 |
| $s_{y/x}$ | 0.036 |
| Degrees of Freedom | 8 |
| SSresidual | 0.011 |
| $R^2$ | 1 |
| F | 18290.06 |
| SSreg | 24.096 |
| sxo | 0.779 |
| $t_{0.05}$ | 2.306 |
| Relative Expanded Uncertainty | 1.795 |
| Error for 241.5 Å$^2$ | 0.743 Å$^2$ |

**Exemplar Structures for Imploded Cryptophanes**



Figure S17: Example imploded structures for $[NH_4+1]^+$: a) exclusion oxygen **D**; b) exclusion bowl **B;** and c) interstitial inclusion **G**.

## Comparison of Gas Phase Findings with ITC and Predicted Thallium behavior

Thallium's toxicity makes it challenging to analyse in the open lab. Instead, globular structures for [Tl+cryptophane]$^+$ where cryptophane = **1** – **4** were optimized by DFT for reaction energy and collisional cross section comparison (Table 7), as the imploded complexes are only relevant for cation = H and Li. Notably, [Tl@Cryptophane]$^+$ structures have very similar $\Omega_{calc}$ to those of the smallest [alkali metal@cryptophane]$^+$ structures. For example, [Na@**1**]$^+$ at 240.3 Å$^2$ and [Tl@**1**]$^+$ at 240.2 Å$^2$ are essentially equal in cross section, while the ionic radius of Tl$^+$ (159 pm) lies between that of K$^+$ and Rb$^+$ (Figure 13). The inclusion complex, [Tl@cryptophane]$^+$, was the lowest relative energy of the [cation@cryptophane]$^+$ series, supporting the conclusion that a globular inclusion complex is preferred. This is consistent with previously reported results that *anti*-cryptophane's interact strongly with Tl$^+$.[19] Similarly, the ITC results presented here give a large equilibrium constant, consistent with strong encapsulation preference. The equilibrium constants given by ITC suggest that Thallium's binding is stronger by orders of magnitude than any of the alkali metals, however Cs$^+$ typically has values of K within 10$^2$ of Tl$^+$. Likewise, the uptake of Tl$^+$ by **7** has been measured to be very low by ITC, due to the bulk of the functional groups (to the point where it could be described as "not binding").[6] Thus, there is agreement between bulk phase techniques and calculated values and the expected behavior of Tl$^+$ with **7** is mimicked by Cs$^+$. This agreement exists despite the differences between the solution phase and the gas phase. In the LiOH/H$_2$O of the ITC solution phase, the deprotonated phenolic oxygens interact with the cations, stabilizing the structure.[4]
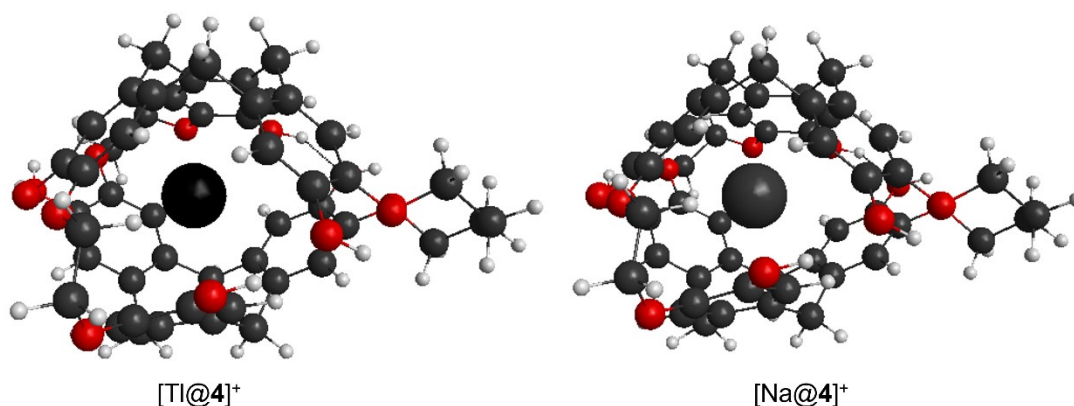


[Tl@**4**]$^+$                    [Na@**4**]$^+$

Figure S18: Thallium and sodium globular inclusion complexes are extremely close in size, despite the difference in cationic radius.

It's expected that the experimentally measured $\Omega$ would be like any alkali metal-cryptophane, complex except Li$^+$. This result is consistent with the known behaviour of Tl$^+$ in biological systems, where it can replace any alkali metal readily, especially K$^+$.[19,20] Surprisingly, however, the ITC results still suggest that Cs$^+$ is the more accurate thermodynamic model, as the magnitude of the equilibrium constants (K in Tables 2 and 3) is closest to Tl$^+$ and the selectivity (regarding encapsulation in **7**) matches more closely. This suggests that the size of a complex as measured by IM-MS is not necessarily linked to the binding strength. This result aligns with our previously stated result that complex size is defined more by the size of the cryptophane and is only impacted a small degree by the internal cation. Tl+cryptophane complexes will be studied by IM-MS in the future.

**Table S8: Calculated reaction energies for thallium as both an exclusion and inclusion complex. $\Omega_{calc}$ values. The lowest $\Delta$E for each species has been bolded.**

| Cryptophane | Cation | Exclusion Aromatic | | Exclusion Oxygen | | Inclusion | |
|---|---|---|---|---|---|---|---|
| | | Calculated $\Delta$E (kJ/mol) | $\Omega_{calc}$ / Å$^2$ | Calculated $\Delta$E (kJ/mol) | $\Omega_{calc}$ / Å$^2$ | Calculated $\Delta$E (kJ/mol) | $\Omega_{calc}$ / Å$^2$ |
| 1 | Tl$^+$ | -181 | 251.1 | -108 | 250.9 | -398 | 240.2 |
| 2 | Tl$^+$ | -232 | 250.6 | -279 | 245.6 | -400 | 243.2 |
| 3 | Tl$^+$ | -189 | 256.3 | -242 | 249.8 | -401 | 245.3 |
| 4 | Tl$^+$ | -184 | 255.2 | -209 | 252.4 | -402 | 246.3 |

Finally, theoretical predictions combined with ITC data presented here suggests that thallium would behave very similarly to the larger alkali metals when measured by ion mobility-mass spectrometry. As such, it is anticipated that the contraction and stability of [Tl@Cryptophane]$^+$ would be readily observed by IM-MS, as predicted by the high equilibrium constants determined for **1** and **4** by ITC. It is expected to form inclusion complexes in the same manner and with similar sizes. Thallium complexes were predicted to be smaller than most alkali metal complexes, perhaps suggesting a stronger binding that induces a slight additional structural contraction. These efforts allow future work to probe the gas-phase structure of thallium complexes safely, simply, and quickly by employing an alkali metal, such as cesium, instead.

# Unscaled Collision Cross Sections

**Table S9: Unscaled collision cross sections calculated for globular structures of 1 - 4.**

| Cryptophane | Cation | Globular Aromatic | Exclusion | Globular Oxygen | Exclusion | Globular Inclusion |
|---|---|---|---|---|---|---|
| | | $\Omega_{org}$ / Å$^2$ | | $\Omega_{org}$ / Å$^2$ | | $\Omega_{org}$ / Å$^2$ |
| 1 | H$^+$ | 271.4 | | 267.8 | | 267.4 |
| | Li$^+$ | 276.6 | | 272.1 | | 267.6 |
| | Na$^+$ | 277.3 | | 270.2 | | 267 |
| | K$^+$ | 280.7 | | 276.8 | | 267.3 |
| | Rb$^+$ | 282.6 | | 278.2 | | 267.6 |
| | Cs$^+$ | 281.9 | | 285.1 | | 268.4 |
| | NH$_4^+$ | 285.3 | | 277.2 | | 268.1 |
| 2 | H$^+$ | 271.7 | | 271.6 | | 270.8 |
| | Li$^+$ | 276.4 | | 270.7 | | 270.6 |
| | Na$^+$ | 277.7 | | 271.2 | | 270.4 |
| | K$^+$ | 281.5 | | 273.4 | | 270.5 |
| | Rb$^+$ | 282.7 | | 274.8 | | 270.9 |
| | Cs$^+$ | 282.7 | | 277 | | 271.6 |
| | NH$_4^+$ | 285 | | 277.7 | | 271.1 |
| 3 | H$^+$ | 281 | | 275.3 | | 279.9 |
| | Li$^+$ | 281.8 | | 278.8 | | 274.1 |
| | Na$^+$ | 282.9 | | 279.9 | | 273.8 |
| | K$^+$ | 287 | | 282.3 | | 274.2 |
| | Rb$^+$ | 287.3 | | 282.9 | | 274.3 |
| | Cs$^+$ | 289.6 | | 283.6 | | 275.2 |
| | NH$_4^+$ | 290.3 | | 283.8 | | 274.5 |
| 4 | H$^+$ | 277.7 | | 280.8 | | 274.6 |
| | Li$^+$ | 287.8 | | 272.7 | | 273.3 |
| | Na$^+$ | 284.4 | | 273.4 | | 273.4 |
| | K$^+$ | 288.4 | | 280 | | 272.9 |
| | Rb$^+$ | 287.9 | | 281 | | 274.3 |
| | Cs$^+$ | 287.4 | | 282.2 | | 275.4 |
| | NH$_4^+$ | 288 | | 282.4 | | 273.6 |

**Table S10: Unscaled collision cross sections calculated for the imploded structures of 1.**

| Cryptophane | Cation | Imploded Exclusion Aromatic $\Omega_{org}$ / Å$^2$ | Imploded Exclusion Oxygen $\Omega_{org}$ / Å$^2$ | Imploded Inclusion $\Omega_{org}$ / Å$^2$ |
|---|---|---|---|---|
| **1** | H$^+$ | 285.7 | 293.5 | 295.4 |
| | Li$^+$ | 295.6 | 289.4 | 292 |
| | Na$^+$ | 292.3 | 290.9 | 292 |
| | K$^+$ | 298.8 | 291.9 | 293.3 |
| | Rb$^+$ | 300.1 | 291.8 | 291.2 |
| | Cs$^+$ | 297.3 | 295.7 | n/a[a] |

**Table S11: Unscaled collision cross sections calculated for the thallium containing globular complexes.**

| Cryptophane | Cation | Imploded Exclusion Aromatic $\Omega_{org}$ / Å$^2$ | Imploded Exclusion Oxygen $\Omega_{org}$ / Å$^2$ | Imploded Inclusion $\Omega_{org}$ / Å$^2$ |
|---|---|---|---|---|
| **1** | Tl$^+$ | 279.0 | 278.8 | 266.9 |
| **2** | Tl$^+$ | 278.4 | 272.9 | 270.2 |
| **3** | Tl$^+$ | 284.8 | 277.6 | 272.6 |
| **4** | Tl$^+$ | 283.5 | 280.4 | 273.7 |

## Partial Charge Schema

IMOS uses a description of partial charges. This information allows a more accurate trajectory method calculation to be performed, as increased charge on an atom will increase the electrostatic interactions (dipole, polarization) experienced when an $N_2$ molecule is nearby. There are several partial charge placement schemes, all of which can be easily implemented during the DFT workflow.

Briefly, early partial charge schemes (such as the Mulliken, Löwdin and Natural population analysis methods) were based on the distribution of atomic orbital occupation. Mulliken partial charges are especially commonly utilized, due to their simplicity of generation and interpretation. However, this method has been known to have issues with strong basis set dependance.[21] Löwdin partial charges have the same fundamental issues as the Mulliken method, such as occasional unphysical partial charges or poor capture of electrostatic moments; however, the partial charge basis set dependence issue is somewhat mitigated compared to Mulliken charge scheme. In contrast, an alternate way of calculating partial charges involves a least-squares fit to the electrostatic potential (ESP). There are a broad range of available ESP based charge schemes, but for the purposes of this small benchmarking study, the oft used and representative CHELPG scheme was used. ESP methods are generally considered to be more accurate than alternative methods, but still occasionally have problematic and unphysical descriptions of atomic partial charges.[22]

Changing the charge placement scheme inherently and significantly changes the actual partial charges output. However, the question remains as to whether the change in the partial charges flows on to affect the calculated collisional cross section of the cryptophanes measured in this work.

To test if the charge placement schema was the root cause of the disparity between experimental single point calculations ($\omega$B97X-D3BJ/def2-TZVPP (ma-def2-TZVPP on all non-hydrogen guest atoms)) were performed with different charge placement schemes for the [K+**1**]$^+$ species; the geometry for all charge calculations was consistent. The partial charges obtained from these calculations were then applied to the same structural coordinates and both projection approximation (PA) and trajectory method (TM) calculations were performed. PA

**Table S12: The comparison between the same structure with different charge placement schema demonstrates the small change in $^{TM}\Omega_{calc}$ whilst not impacting the $^{PA}\Omega_{calc}$.**

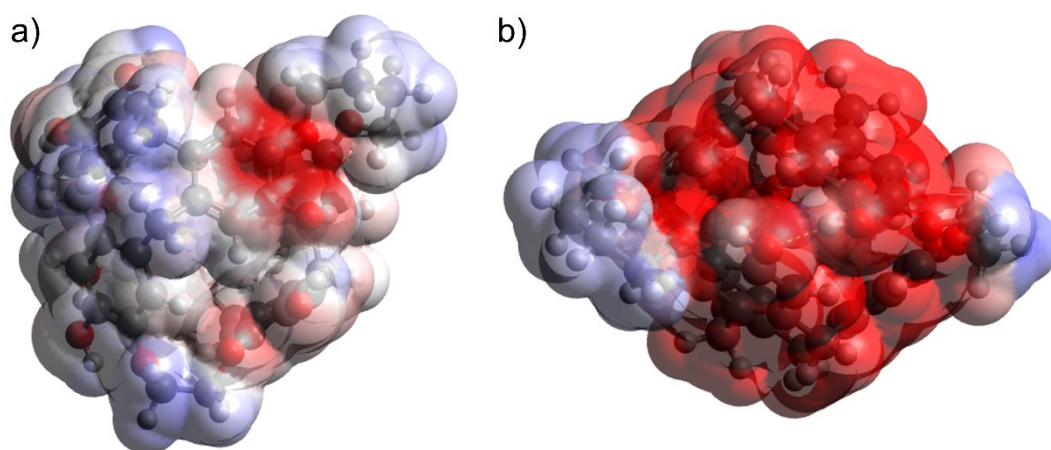| Charge Placement Scheme | Inclusion | | Exclusion Oxygen | |
|---|---|---|---|---|
| | $^{PA}\Omega_{calc}$ | $^{TM}\Omega_{calc}$ | $^{PA}\Omega_{calc}$ | $^{TM}\Omega_{calc}$ |
| Mulliken | 186.0 | 267.3 | 198.5 | 276.8 |
| Löwdin | 186.0 | 266.6 | 198.5 | 276.7 |
| CHELPG | 186.0 | 267.1 | 198.5 | 277.5 |



Figure S19: A comparison of electrostatic surface plots between a) a proton and b)sodium inclusion complexes (with **4**). This reveals the far less homogenous charge distribution of proton complexes compared to the larger cations,
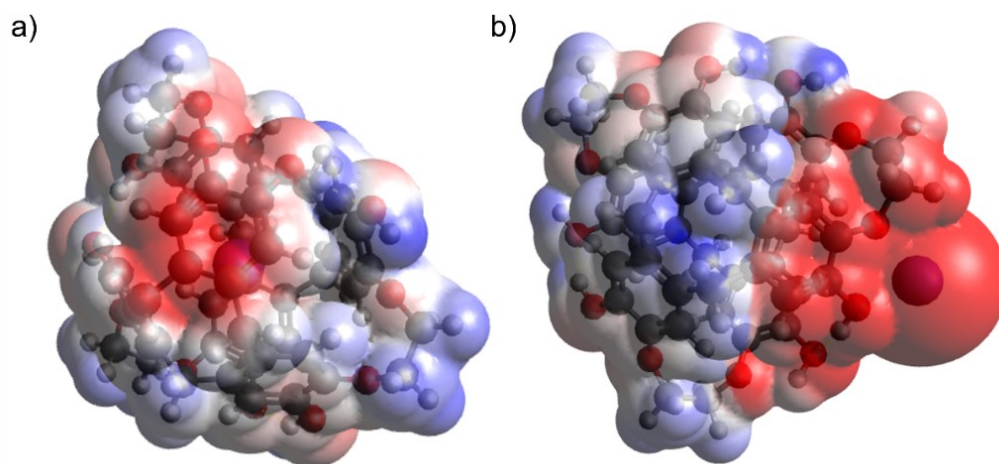
Figure S20: A comparison of electrostatic surface plots between a) an inclusion and b) exclusion complex reveals the significant difference in partial charge that will significantly impact the interaction with the drift gas.

**Table S13: The calculated reaction energies (ΔE) and collision cross sections ($\Omega_{calc}$) for positional isomers of the globular [H+cryptophane]$^+$ complexes 2- 4.**

| Cryptophane | Cation | A Globular Inclusion | | C Globular Exclusion Oxygen | | E Globular Exclusion Aromatic | |
| | | Calculated ΔE / kJ mol$^{-1}$ | $\Omega_{calc}$ / Å$^2$ | Calculated ΔE / kJ mol$^{-1}$ | $\Omega_{calc}$ / Å$^2$ | Calculated ΔE / kJ mol$^{-1}$ | $\Omega_{calc}$ / Å$^2$ |
|---|---|---|---|---|---|---|---|
| 2 | H$^+$ | -956[a] | 243.7 | -925[a] | 244.4 | -974[a] | 244.5 |
| 3 | H$^+$ | -949[a] | 251.9 | -931[a] | 247.8 | -904[a] | 252.9 |
| 4 | H$^+$ | -887[a] | 247.1 | -937[a] | 252.7 | -901[a] | 249.9 |

*a* As noted, proton ΔE values are significantly larger in magnitude as the complexes formed are covalent cryptophane carbocations and are not structural analogues to other cationic association complexes and cation-π complexes.

## Volume Calculation Validity

The volumes determined for the cryptophanes were distinctly smaller than those reported in the literature, which are often in the range of 100 Å$^3$.[23–25] This is somewhat expected, as a molecule existing in the gas phase will generally contract, however the size disparity was great enough to warrant an examination of the results.

One approach that was used in literature was the cavity surface tool in Swiss-Pdb Viewer.[23] This tool detects cavities and builds polygonal 3D surfaces within them, taking account of Van der Waals radii. When reimplemented on a cryptophane from the original literature, a similar value was obtained. However, when implemented on the smaller cryptophanes, such as **1**, Swiss-Pdb Viewer could not detect a cavity, and so would not output a cavity volume, not matter what "quality" setting was used. When implemented on a slightly larger cryptophane, 4, the internal cavity was detected and was found to be 24 Å$^3$. When the convex hull method is applied to the same molecule, a value of 28 Å$^3$ was obtained. This similarity demonstrates that the new approach suggested in this work has a place in the analytical toolkit, especially when smaller cavities are apparent.

As the results presented in this work are based on DFT, they should not be used to discount experimental values generated from solid-phase data. The reverse is also true, as solid-phase data is not an accurate description of the structure as it exists in the gas-phase.
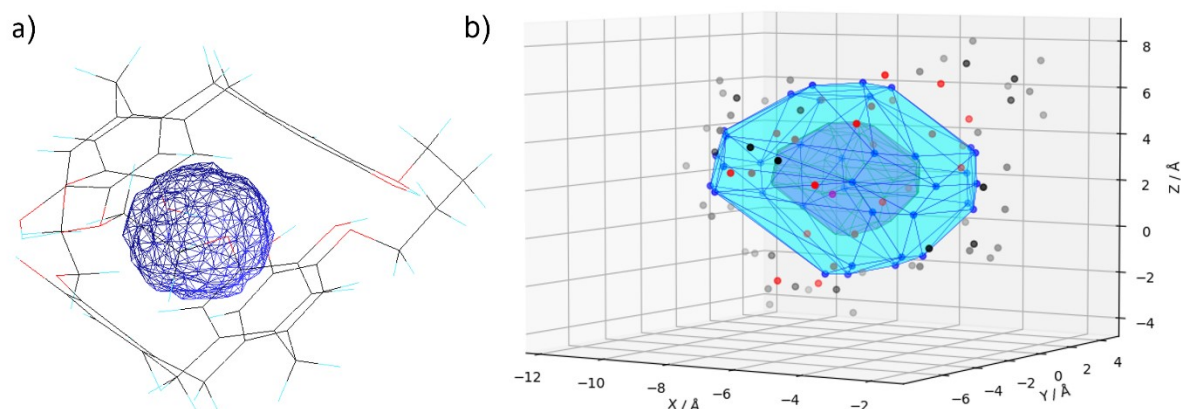


Figure S21: The comparison between a) the cavity surface generated by Swiss-PDB Viewer and b) the convex hull (pink) created using method presented in this work.

## Extension to Cryptophanes 5, 6 and 7.

The volume trends for cation = Na$^+$, K$^+$, Rb$^+$, Cs$^+$ or NH$_4^+$ can be extended to **5** and **6,** due to their structural similarity with **1 – 4.** However, extrapolation is not appropriate for **7** because there is a known departure from the trend for cation = NH$_4^+$ and Cs$^+$. For imploded structures or structures where the steric bulk of groups, e.g. the carboxylic groups in **7**, can limit encapsulation of larger cations,[20] the cavity of the cryptophane can be significantly reduced in size, effectively "self-solvating" the interior of the cryptophane, and as such, the current cavity approach is not applicable in those cases.

**Cavity volume approach applied to the globular exclusion aromatic structures E**
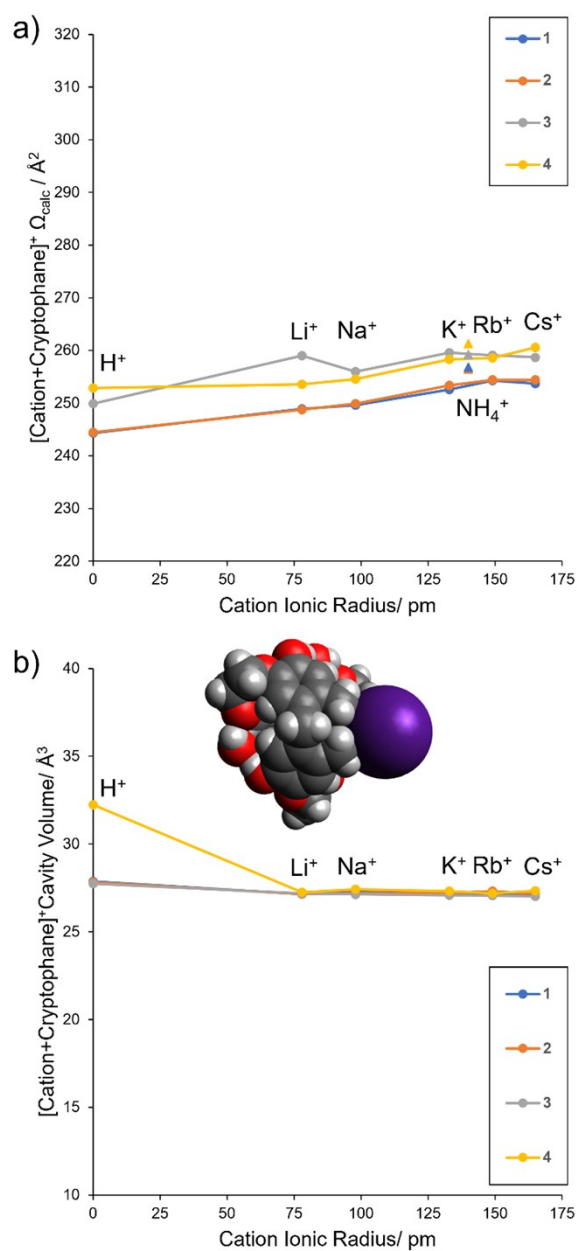


Figure S22: The predicted collision cross sections for globular complexes of **1-4** when the Group 1 cation is a) an association complex at the Aromatic position.; b) The calculated volume of the cryptophane cavity remains almost constant when the cation is external.

When the cavity volume approach is applied to the globular exclusion aromatic structures E, the variation is minimal (Figure 22 b). The variation in cation does not impact the globular structure of the cryptophane when in an external association complex. Experimentally, if any cation $Na^+$-$Cs^+$ were external, both the increased interaction of the cation with the drift gas, along with the ionic radius of the cation would increase $\Omega$ without any offset. This is not experimentally observed. Therefore, along with cross sections and relative energetics of the optimized structures, the calculated cavity volumes are further supporting evidence that the globular inclusion (Figure 5 **A**) is preferred and occurs when cation = $Na^+$, $K^+$, $Rb^+$, $Cs^+$ or $NH_4^+$ for cryptophanes **1-4**.

## SI References

(1)      Bouchet, A.; Brotin, T.; Cavagnat, D.; Buffeteau, T. Induced Chiroptical Changes of a Water-Soluble Cryptophane by Encapsulation of Guest Molecules and Counterion Effects. *Chem. – Eur. J.* **2010**, *16* (15), 4507–4518. https://doi.org/10.1002/chem.200902740.

(2)      Brotin, T.; Goncalves, S.; Berthault, P.; Cavagnat, D.; Buffeteau, T. Influence of the Cavity Size of Water-Soluble Cryptophanes on Their Binding Properties for Cesium and Thallium Cations. *J. Phys. Chem. B* **2013**, *117* (41), 12593–12601. https://doi.org/10.1021/jp4074009.

(3)      Bouchet, A.; Brotin, T.; Linares, M.; Cavagnat, D.; Buffeteau, T. Influence of the Chemical Structure of Water-Soluble Cryptophanes on Their Overall Chiroptical and Binding Properties. *J. Org. Chem.* **2011**, *76* (19), 7816–7825. https://doi.org/10.1021/jo201167w.

(4)      Chapellet, L.-L.; Dognon, J.-P.; Jean, M.; Vanthuyne, N.; Berthault, P.; Buffeteau, T.; Brotin, T. Experimental and Theoretical Study of the Complexation of Cesium and Thallium Cations by a Water-Soluble Cryptophane. *ChemistrySelect* **2017**, *2* (19), 5292–5300. https://doi.org/10.1002/slct.201700979.

(5)      Chapellet, L.-L.; Cochrane, J. R.; Mari, E.; Boutin, C.; Berthault, P.; Brotin, T. Synthesis of Cryptophanes with Two Different Reaction Sites: Chemical Platforms for Xenon Biosensing. *J. Org. Chem.* **2015**, *80* (12), 6143–6151. https://doi.org/10.1021/acs.joc.5b00653.

(6)      Brotin, T.; Berthault, P.; Pitrat, D.; Mulatier, J.-C. Selective Capture of Thallium and Cesium by a Cryptophane Soluble at Neutral pH. *J. Org. Chem.* **2020**, *85* (15), 9622–9630. https://doi.org/10.1021/acs.joc.0c00950.

(7)      Brotin, T.; Dutasta, J.-P. Xe@cryptophane Complexes with C2 Symmetry: Synthesis and Investigations by 129Xe NMR of the Consequences of the Size of the Host Cavity for Xenon Encapsulation. *Eur. J. Org. Chem.* **2003**, *2003* (6), 973–984. https://doi.org/10.1002/ejoc.200390153.

(8)      Robert E. Ireland; David M. Walba. Demethylation of Methyl Aryl Ethers: 4-Ethoxy-3-Hydroxybenzaladehyde. *Org. Synth.* **1977**, *56* (44). https://doi.org/10.15227/orgsyn.056.0044.

(9)      Giles, K.; Ujma, J.; Wildgoose, J.; Pringle, S.; Richardson, K.; Langridge, D.; Green, M. A Cyclic Ion Mobility-Mass Spectrometry System. *Anal. Chem.* **2019**, *91* (13), 8564–8573. https://doi.org/10.1021/acs.analchem.9b01838.

(10)    Neese, F. The ORCA Program System. *WIREs Comput. Mol. Sci.* **2012**, *2* (1), 73–78. https://doi.org/10.1002/wcms.81.

(11)    Mehta, N.; Abrahams, B. F.; Goerigk, L. Clam-like Cyclotricatechylene-Based Capsules: Identifying the Roles of Protonation State and Guests as Well as the Drivers for Stability and (Anti-)Cooperativity. *Chem. – Asian J.* **2020**, *15* (8), 1301–1314. https://doi.org/10.1002/asia.201901767.

(12)    Larriba-Andaluz, C.; Hogan, C. J., Jr. Collision Cross Section Calculations for Polyatomic Ions Considering Rotating Diatomic/Linear Gas Molecules. *J. Chem. Phys.* **2014**, *141* (19), 194107. https://doi.org/10.1063/1.4901890.

(13)    Ouyang, H.; Larriba-Andaluz, C.; Oberreit, D. R.; Hogan, C. J. The Collision Cross Sections of Iodide Salt Cluster Ions in Air via Differential Mobility Analysis-Mass Spectrometry. *J. Am. Soc. Mass Spectrom.* **2013**, *24* (12), 1833–1847. https://doi.org/10.1007/s13361-013-0724-8.

(14)    Larriba, C.; Hogan, C. J. Free Molecular Collision Cross Section Calculation Methods for Nanoparticles and Complex Ions with Energy Accommodation. *J. Comput. Phys.* **2013**, *251*, 344–363. https://doi.org/10.1016/j.jcp.2013.05.038.

(15)    Larriba, C.; Hogan, C. J. Jr. Ion Mobilities in Diatomic Gases: Measurement versus Prediction with Non-Specular Scattering Models. *J. Phys. Chem. A* **2013**, *117* (19), 3887–3901. https://doi.org/10.1021/jp312432z.

(16)    Geue, N.; Bennett, T. S.; Arama, A.-A.-M.; Ramakers, L. A. I.; Whitehead, G. F. S.; Timco, G. A.; Armentrout, P. B.; McInnes, E. J. L.; Burton, N. A.; Winpenny, R. E. P.; Barran, P. E. Disassembly Mechanisms and Energetics of Polymetallic Rings and Rotaxanes. *J. Am. Chem. Soc.* **2022**, *144* (49), 22528–22539. https://doi.org/10.1021/jacs.2c07522.

(17)    Maglic, J. B.; Lavendomme, R. It MoloVol: An Easy-to-Use Program for Analyzing Cavities, Volumes and Surface Areas of Chemical Structures. *J. Appl. Crystallogr.* **2022**, *55* (4), 1033–1044. https://doi.org/10.1107/S1600576722004988.

(18)    Bush, M. F.; Campuzano, I. D. G.; Robinson, C. V. Ion Mobility Mass Spectrometry of Peptide Ions: Effects of Drift Gas and Calibration Strategies. *Anal. Chem.* **2012**, *84* (16), 7124–7130. https://doi.org/10.1021/ac3014498.

(19)    Galván-Arzate, S.; Santamaría, A. Thallium Toxicity. *Toxicol. Lett.* **1998**, *99* (1), 1–13. https://doi.org/10.1016/S0378-4274(98)00126-X.

(20)     Titus, S. A.; Beacham, D.; Shahane, S. A.; Southall, N.; Xia, M.; Huang, R.; Hooten, E.; Zhao, Y.; Shou, L.; Austin, C. P.; Zheng, W. A New Homogeneous High-Throughput Screening Assay for Profiling Compound Activity on the Human Ether-a-Go-Go-Related Gene Channel. *Anal. Biochem.* **2009**, *394* (1), 30–38. https://doi.org/10.1016/j.ab.2009.07.003.

(21)     North, S. C.; Jorgensen, K. R.; Pricetolstoy, J.; Wilson, A. K. Population Analysis and the Effects of Gaussian Basis Set Quality and Quantum Mechanical Approach: Main Group through Heavy Element Species. *Front. Chem.* **2023**, *11*.

(22)     Ongari, D.; Boyd, P. G.; Kadioglu, O.; Mace, A. K.; Keskin, S.; Smit, B. Evaluating Charge Equilibration Methods To Generate Electrostatic Fields in Nanoporous Materials. *J. Chem. Theory Comput.* **2019**, *15* (1), 382–401. https://doi.org/10.1021/acs.jctc.8b00669.

(23)     Taratula, O.; Hill, P. A.; Khan, N. S.; Carroll, P. J.; Dmochowski, I. J. Crystallographic Observation of "induced Fit" in a Cryptophane Host–Guest Model System. *Nat. Commun.* **2010**, *1* (1), 148. https://doi.org/10.1038/ncomms1151.

(24)     Mecozzi, S.; Rebek, Jr., Julius. The 55 % Solution: A Formula for Molecular Recognition in the Liquid State. *Chem. – Eur. J.* **1998**, *4* (6), 1016–1022. https://doi.org/10.1002/(SICI)1521-3765(19980615)4:6<1016::AID-CHEM1016>3.0.CO;2-B.

(25)     Fogarty, H. A.; Berthault, P.; Brotin, T.; Huber, G.; Desvaux, H.; Dutasta, J.-P. A Cryptophane Core Optimized for Xenon Encapsulation. *J. Am. Chem. Soc.* **2007**, *129* (34), 10332–10333. https://doi.org/10.1021/ja073771c.